Supporting Information

An Aqueous Route to Phthalocyanine–Fullerene Composites with Regular Structure

N. Yu. Borovkov, A. M. Kolker

Abbreviations

CoPc$^{\#}$, cobalt *tetrakis*(3-amino-5-*tert*-butyl)phthalocyanine

CoPc*, cobalt *tetrakis*(3-nitro-5-*tert*-butyl)phthalocyanine

Content

Part I. General Features of CoPc#

The dye under investigation is depicted in **Figure S1**; its optical spectra are shown in **Figure S2**.

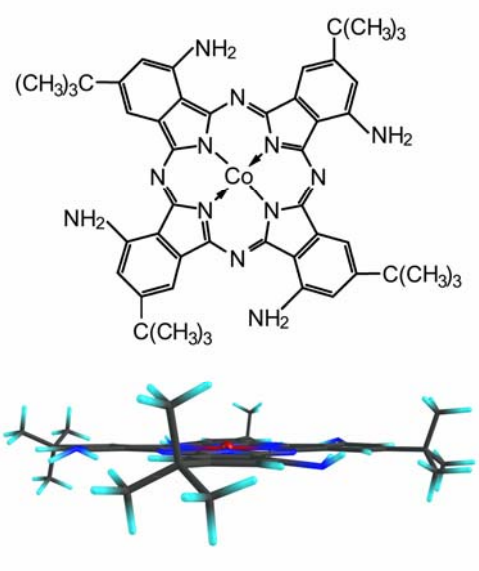

Figure S1. Aminophthalocyanine CoPc# (the C_{4h}-isomer) and its molecular geometry (side view). Atom colors: C, black; H, cyan; N, blue; Co, red.

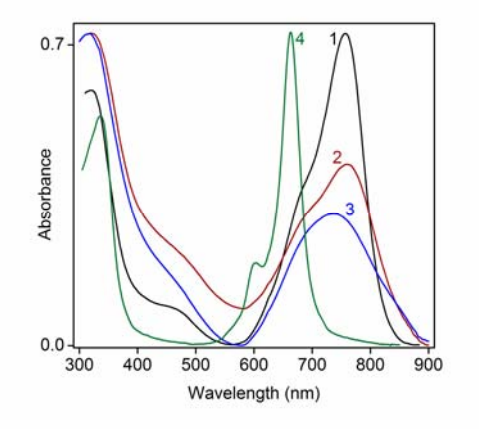

Figure S2. Optical spectra of CoPc#: curve 1, in benzene; curve 2, in a freshly cast film; curve 3, in a cast film aged. A spectrum of the nitro-substituted parent dye CoPc* in benzene (curve 4) is given for comparison. The molar extinction in solution is 1.2 10^4 M^{-1} cm^{-1} at 758 nm.

When cast from hydrophobic organic solvents, translucent CoPc# films decorated with cracks and holes are obtained (**Figure S3**).

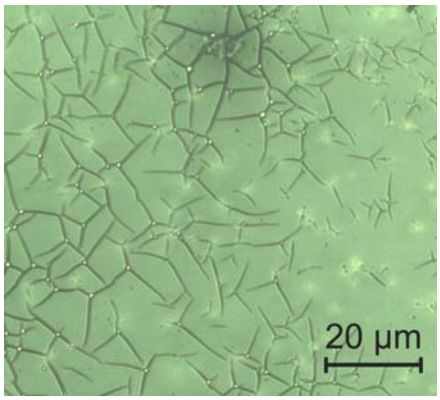

Figure S3. Optical microscopy image of the benzene-cast CoPc# film.

Figure S4 shows SAXS data on the cast film. The trace was recorded on the AMUR-K diffractometer [S1] using the Cu Kα radiation (λ = 1.54 Å). It has a wide peak corresponding to the 1-stack aggregate (insert), in which the stacked molecules are shifted and, as a result, tilted at ca. 50 ° relative to the glass surface.

Structural ordering in thin films is characterized by the correlation length, *L*, obtained from the Scherrer formula $L = 50.93\lambda/(\eta \cdot \cos\Theta)$, where λ is the X-ray wavelength (nm), η is the full width of the peak at half-maximum intensity (deg), Θ is

the Bragg angle (deg). So, the *L* value in the film was estimated as ca. 10 nm, i.e., seven 1-stack units.

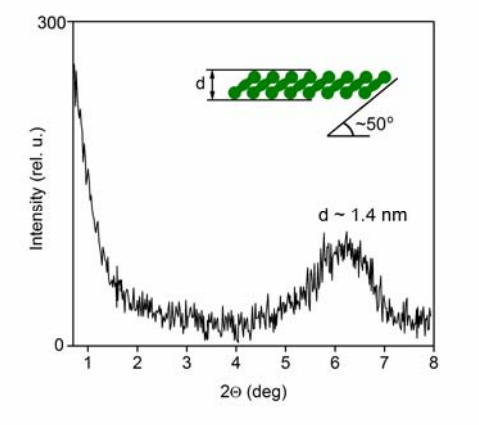

Figure S4. Small-angle X-ray diffraction pattern of the CoPc$^{\#}$ film shown in **Figure S3**. The insert shows a supposed structure of the 1-stack aggregate.

Valuable physicochemical information was acquired by comparison of WAXS data on powdery samples of CoPc$^{\#}$ and CoPc*. Because the two samples are identical mixtures of four geometric isomers, all structural differences between CoPc$^{\#}$ and CoPc* may be interpreted in terms of the energy balance between the polar van der Waals interactions (typical for CoPc$^{\#}$) and the π–π coupling (typical for CoPc*).

Figure S5 shows the WAXS data acquired on a Bruker P4 diffractometer (MA, USA) using the Mo Kα radiation (λ = 0.711 Å). The peaks were assigned by analogy with the work [S2]. The peak 1 corresponds to the height of the 1-stack aggregate (**Figure S4**, insert). Its profile indicates that the CoPc$^{\#}$ aggregates are aligned by far poorer than the CoPc* ones. The peak 2 corresponds to the diameter of the *tert*-butyl group (ca. 0.6 nm). The peak 3 is not identified so far. The peak 4 corresponds to the 1D stacking of the peripheral benzene fragments.

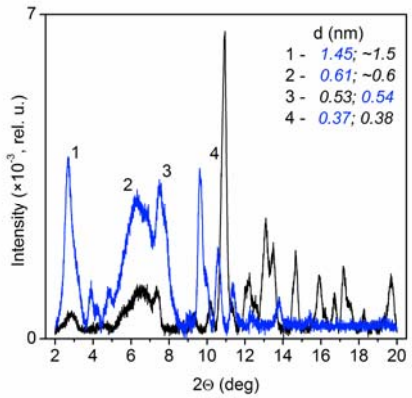

Figure S5. X-Ray powder diffraction patterns of CoPc$^{\#}$ (black) and CoPc* (blue). Both samples were precipitated from benzene and desolvated at room temperature under reduced pressure. Common peaks are numbered.

Of primary interest is the last peak: it indicates that the CoPc$^{\#}$ aggregate is more compact than the CoPc* one. This fact appears to be in contradiction with the poor alignment of the aggregates and may be rationalized as follows. In the case of CoPc$^{\#}$, both inter-molecular and inter-aggregate interactions are driven by H bonding. Multiple (up to four) H bonds between the CoPc$^{\#}$ molecules produce a more efficient attraction than the π-stacking interaction between the sterically hindered CoPc* molecules. The H bonds

operate also at the inter-aggregate level, making the CoPc# aggregates to clutch one another in a random manner and, thus, hindering the alignment.

Part II. CoPc# and C_{60} at the Air–Water Interface

Behavior of CoPc# at the air–water interface was studied on a rectangular Teflon trough (NT–MDT, Russia). All compression curves were recorded strictly within 18–20 °C.

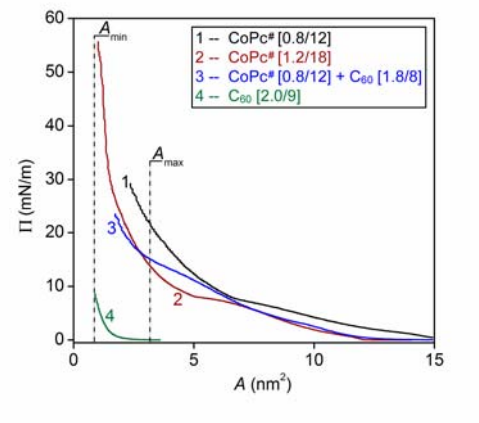

Figure S6. Compression curves for the floating layers of CoPc# and C_{60}. Initial surface concentration ($N_0 \times 10^7$, mol/m^2) and corresponding initial surface coverage (C_0, %) are given in brackets as [N_0/C_0]. The A_{min} and A_{max} symbols stand for the smallest and largest areas the CoPc# molecule can occupy in the monolayer.

Figure S6 shows the surface pressure vs. area per molecule (Π–*A*) curves for two layers prepared at initial surface coverage C_0 of 12% and 18% (the curves 1 and 2). In both cases, the pressure starts rising at very large effective areas per molecule (ca. 18 nm^2 and ca. 14 nm^2, respectively), whereas the maximal area the CoPc# molecule can occupy at the interface is estimated as 3.2 nm^2 at best (A_{max} in **Figure S6**). The Π–*A* curves diverge at Π of ca. 7 mN/m, indicating two different aggregation routes at higher surface pressures. Inflections on the curves are indistinct and hardly explicable in a straightforward manner. Therefore we used the approach [S3,S4], which allowed extracting quantitative information even from outwardly featureless curves.

Our procedure consists of two steps. First, one constructs Π*A*–Π plots and finds inflection points. Second, one associates these points with pressure-induced structural events at the interface. To make the second step, a set of molecular areas is needed (**Figure S7**).

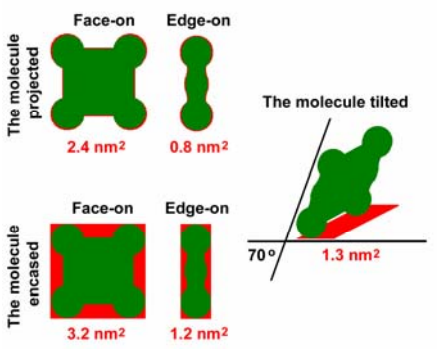

Figure S7. The areas (A_{mol} in red) the CoPc# molecule can occupy on the water surface (see the work [S3] for details).

An easy case for analysis is the most rarefied layer prepared at C_0 of 12% (**Figure S8**). The Π*A*–Π plot has a short linear portion *C*–*D* ranging from ca. 7.5 to 11.0 mN/m. The portion has a slope of (2.41 ± 0.03) nm^2 being strictly equal to the area of the molecular face. Thus, there exists a one-phase monolayer of the dye molecules lying face-on on the water surface. The difference (4.4 nm^2) between the effective area at the point *C* (6.8 nm^2) and the molecular area in the monolayer phase (2.4 nm^2) belongs to the hydration shell tightly bound to the dye molecule. The next portion *D*–*E* corresponds to the slowly collapsing monolayer.

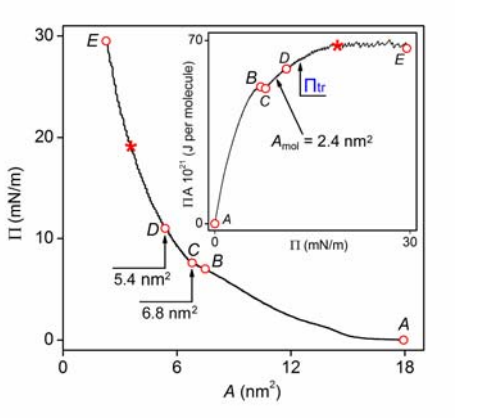

Figure S8. The compression curve for the CoPc$^{\#}$ layer (C_0 = 12%) with inflection points extracted from the corresponding Π*A*–Π plot (insert). The onset of the isothermal compression stage is marked with an asterisk. Π_{tr} is transfer pressure.

The face-on arrangement shows first symptoms of instability at the point *D*. So, the minimal size of the stable hydration shell is estimated as the difference between the effective area at the point *D* (5.4 nm^2) and the slope (2.4 nm^2). It is close to 3 nm^2.

The Π*A* quantity is a work of layer compression; hence, the Π*A*–Π relationship is generally determined by the energy balance between the pressure-induced disruption and formation of intermolecular non-covalent bonds. As a result, a normal Π*A*–Π plot consists of variously curved portions corresponding to either endo- or exothermic processes in a layer. In the case under consideration, the compression becomes isothermal starting from Π of ca. 19 mN/m (marked with an asterisk), indicating a lack of physicochemical processes, both endothermic dehydration and exothermic aggregation, at the final compression stage.

The first portion *A*–*B* corresponds to the expanded monolayer, where the individual dye molecules coexist with the water clusters acting as a second interfacial phase. It ranges from 0 to 7.0 mN/m (point *B*). The difference (ca. 11 nm^2) between the effective areas at the points *A* (18 nm^2) and *C* (6.8 nm^2) belongs solely to the clusters. Thus, the surface effect of hydrophobic hydration may be estimated as ca. 3 nm^2 of the structured water per one *tert*-butyl group.

A more instructive case is the layer prepared at C_0 of 18% (**Figure S9**). Here

one observes two linear portions on the Π*A*–Π plot: *D*–*E* ranging from 9.5 to 16.0 mN/m and *F*–*G* ranging from 29.0 to 50.5 mN/m. Both have the slope of (0.65 ± 0.01) nm^2. The linear portions are separated by the slightly domed one *E*–*F*. Thus, there exist two interfacial phases, which are similar structurally and energetically. The slope value indicates that the layers are bimolecular, while the dye molecules are tilted at ca. 70 ^{o} relative to the water surface (**Figure S7**). Evidently the higher bilayer phase (portion *F*–*G*) arises as a result of the in-plane consolidation of the 2-stack aggregates, which have been assembled at the lower aggregation stage (portion *D*–*E*). So, the portion *E*–*F* may be ascribed to a zone of the order–disorder transition, where the H bonds of hydration are being substituted with the inter-aggregate H bonds. The last portion *G*–*H* corresponds to the abruptly collapsing bilayer. The difference (ca. 3.6 nm^2) between the effective area at the point *D* (4.2 nm^2) and the molecular area in the bilayer phase (0.65 nm^2) is attributable to the hydration shell of the 2-stack aggregate.

Similar to the more rarefied layer analyzed above, the portion *A*–*B* corresponds to the monolayer expanded by the water clusters. It also ranges from 0 to 7.0 mN/m, but the effective area at Π of 7.0 mN/m (point *B*) is only 6.5 nm^2 as against 7.5 nm^2 in the former case. This contraction is achieved at the expense of the hydration shell, which is partially lost due to the dye aggregation in the free-floating layer. Although it is small (< 15%), it suffices to promote the abrupt aggregation when Π increases from 7.0 to only 8.3 mN/m. The corresponding portion *B*–*C* on the Π*A*–Π plot is linear with a huge negative slope of (-6.0 ± 0.1) nm^2, indicating a strongly exothermic process driven obviously by the π-stacking interaction. Metaphorically such a phenomenon may be called *the inverted domino effect*.

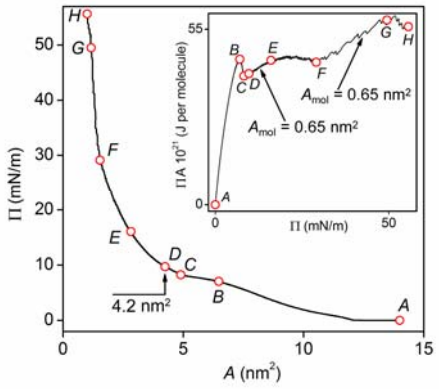

Figure S9. The compression curve for the CoPc$^{\#}$ layer (C_0 = 18%) with inflection points extracted from the corresponding Π*A*–Π plot (insert).

Figure S10 summarizes the discussed structural features of the CoPc$^{\#}$ layers. A key feature of the layers is two kinds of dye-modified surface water. The hydration water (yellow) is caused by hydrophilic hydration of four primary amine groups and, hence, is tightly bound to the CoPc$^{\#}$

molecule. The clustered water (orange) results from the effect of hydrophobic hydration produced by the long-range attraction of the *tert*-butyl-groups across water [S5]. The water clusters span the gaps between the hydrophobic molecular rims [S6] and, thus, behave as a second interfacial phase expanding the CoPc# layers at low surface pressures.

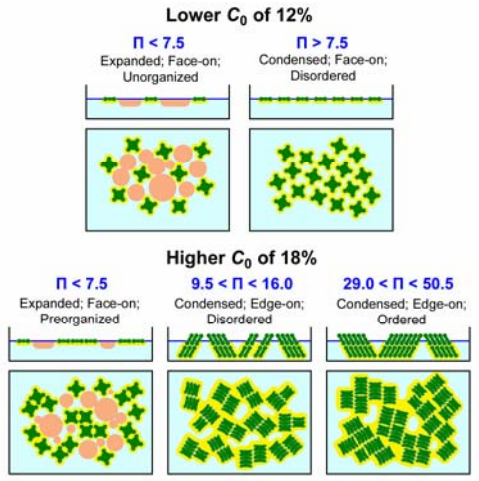

Figure S10. Schematic of the CoPc# layers on the water surface (side and top views) at various conditions. Color code: CoPc#, green; amorphous H_2O, cyan; clustered H_2O, orange; bound H_2O, yellow.

The free-floating layer prepared at lower C_0 is ideal gaseous: the CoPc# molecules are randomly distributed over the surface and surrounded by hydration shells. As a result, they are mutually isolated and unable to aggregate. The less rarified layer is non-ideal at zero Π, because it contains proto-aggregates. The proto-aggregates act as seeds for the π-stacked aggregates, which firstly appear at Π of ca. 7 mN/m. The latter have 2-stack architecture, the stacked molecules being shifted and, therefore, tilted at ca. 70 ^{o} relative to the water surface. Severe compression makes the 2-stack aggregates to align, thus yielding a compact bimolecular layer stable up to Π of 50 mN/m.

The ideal monolayer was used to deposit Langmuir–Schaeffer (LS) films at surface pressure of 12 mN/m (Π_{tr} in **Figure S8**). The 90-layer film was studied using SAXS (**Figure S11**) and polarized optical spectroscopy (**Figure S12**).

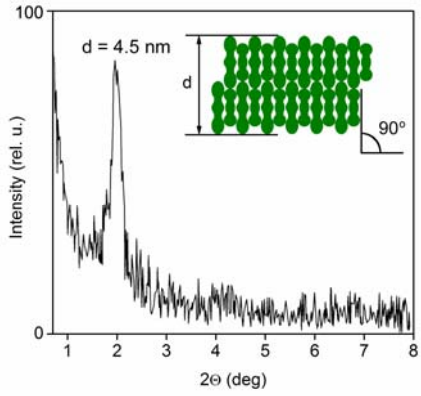

Figure S11. Small-angle X-ray diffraction pattern of the LS film of CoPc# (90 layers) on glass. The insert illustrates the 2-stack architecture of the dye aggregate.

The SAXS data confirms directly that the 2-stack architecture of the dye aggregate is not merely stabilized by the hydration water but inherently stable. Probing the LS film with polarized optical spectroscopy shows that the solid dye aggregate exhibits two transition moments crossing at a large angle. The main transi-

tion (840 nm) is parallel to the film surface while the other (780 nm) is tilted. The latter transition is not detected at the angle of incidence of 45°, indicating that the light-absorbing aggregates are poorly oriented in the vertical direction.

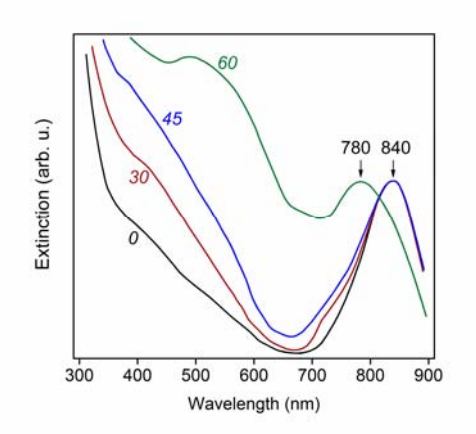

Figure S12. Normalized polarized optical spectra of CoPc$^{\#}$ in the LS film (90 layers) recorded at different angles of incidence (italic numbers).

Next we examined a mixed CoPc$^{\#}$–C_{60} layer with the CoPc$^{\#}$/C_{60} ratio of ca. 1:2.2, mol. The mixed layer was prepared by a two-step procedure. Initially the dilute CoPc$^{\#}$ solution in chloroform (0.3 mM) was spread onto the water surface to prepare a layer with C_0 of 12% and N_0 of 0.8×10^{-7} mol/m^2. Then the saturated C_{60} solution in cyclohexene (0.9 mM) was spread over the dye-covered water surface to obtain the mixed layer with the CoPc$^{\#}$/C_{60} ratio of 1:2.2, mol. After solvent evaporation, the hydrophobic C_{60} molecules submerged and the submonolayer constructed from the water-encapsulated C_{60} molecules arose. [S7] The corresponding compression curve (**Figure S6**, curve 3) nearly overlaps the curves for the CoPc$^{\#}$ layers (the curves 1 and 2) but has little in common with the curve for the pristine C_{60} one (the curve 4). Thus, the mixed layer structure is determined by the buoyant amphiphile, while the submerged hydrophobic component plays a notably minor role. The curve 3 (**Figure S6**) is explicated in **Figure S13**.

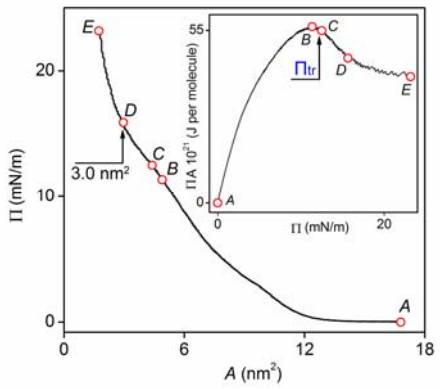

Figure S13. The compression curve for the mixed layer CoPc$^{\#}$–C_{60} (1:2.2, mol) with inflection points extracted from the corresponding Π*A*–Π plot (insert). Π_{tr} is transfer pressure.

Of special interest is the short linear portion *C*–*D*, which ranges from 12.5 to 16.0 mN/m and has a negative slope of (-2.72 ± 0.03) nm^2. This slope indicates two items. First, the exothermic process of dye aggregation really occurs. Second, the aggregation is driven by a noticeably weaker interaction than the π-stacking, the best candidate for the driving force being the short-

range hydrophobic attraction between the *tert*-butyl groups of adjacent dye molecules. The effective area at the point *D* (3.0 nm^2) is close to the calculated area per one encased CoPc# molecule lying face-on on the water surface (3.2 nm^2 in **Figure S7**).

The said structural features of the mixed layer are summarized in **Figure S14**.

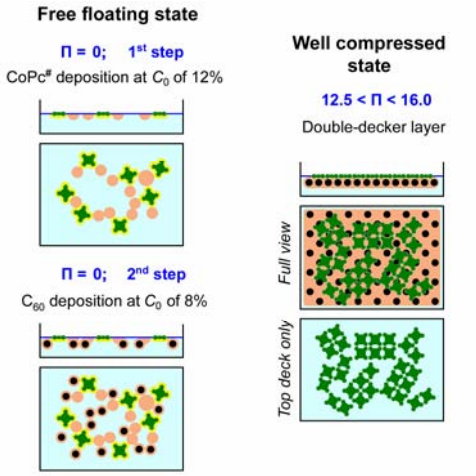

Figure S14. Schematic of the mixed CoPc#–C_{60} layer (1:2.2, mol). Color code as in **Figure S10**; the C_{60} molecules are drawn with black.

A last question to be answered is why the CoPc# layer does not gain the stacked structure when compressed in the presence of fullerene C_{60}?

In the ideal gaseous layer (**Figure S15**, left), the dye molecules are randomly distributed over the surface. The hydration shell is tightly bound to the molecule and cannot be removed by purely physical means. As a result, even severe compression is ineffective against the layer ideality: the system sooner gets collapsed than adopts the habitual stacked structure.

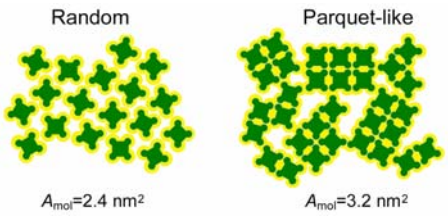

Figure S15. Two kinds of the in-plane structure in the CoPc# monolayer (top view). The hydration water is drawn with yellow.

In the non-ideal layer (**Figure S15**, right), there exist the proto-aggregates, which consist of a few molecules bound together by the hydrophobic attraction. This interaction makes the molecules to align edge-to-edge; so, the proto-aggregates adopt the parquet-like structure and are ready for the π-stacking upon further compression.

In the mixed layer, the dye molecules rest over the molecular capsules $C_{60}@(H_2O)_n$ ($n > 60$). The negative slope of the linear portion *C–D* (**Figure S13**) plainly shows that the hydration shell of the dye molecule does not dissociate during compression. Instead, the monolayer undergoes a downward drainage of the dye-bound water with no enthalpic loss. The drainage is allowed to consume no energy because the C_{60} sub-monolayer and CoPc# monolayer are interlinked by the clustered water, while the former has a higher capacity for water. Severe compres-

sion (**Figure S13**, portion *D*–*E*) cracks the molecular parquet and the "naked" $CoPc^{\#}$ molecules, which are now securely attached to the capsules $C_{60}@(H_2O)_n$, randomly move apart without a chance for the π-stacking.

Part III. $CoPc^{\#}$ Simulated

Molecular modeling was performed by the PM3 method at the CNDO level using the software package HyperChem 5. [S8,S9]

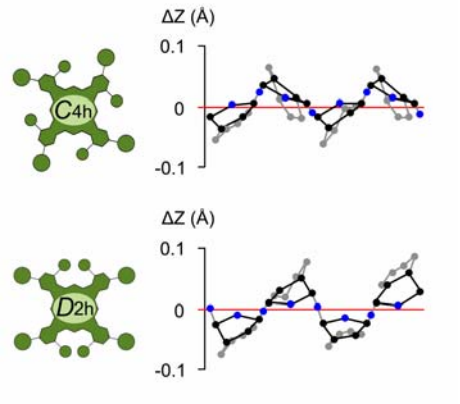

Figure S16. Linear representations of two $CoPc^{\#}$ isomers. Color code: pyrrolic C, black; pyrrolic N, blue; benzene C, gray. The substituents are omitted.

As a first step, the molecular geometry of two isomers, the isometric C_{4h} and anisometric D_{2h} ones, was optimized. Deviations from the molecular planarity are shown in **Figure S16**. Both molecules suffer the saddle-like distortion. An average displacement of the pyrrolic atoms from the equatorial plane was calculated as 0.022 Å and 0.035 Å for the C_{4h} and D_{2h} isomers, respectively. Thus, both molecules are planar to within 0.1 Å (ca. 1.5% of the buckyball diameter) and no steric contribution to the $CoPc^{\#}$–C_{60} interaction is expected.

Next the simplest $CoPc^{\#}$ aggregates were simulated. Two identical $CoPc^{\#}$ molecules were placed next to each other in a shish kebab mode. A value of the rotation angle φ was preset as 0 for the fully eclipsed configuration and as 45° for the fully staggered one. Optimization was performed by the steepest-descent method until the gradient in minimization algorithm had reached a value of 0.005 kJ/(mol Å). Four characteristics of the aggregates were calculated (see *Abbreviations* for **Table**). The minimal and maximal Pc–Pc distances were determined as a vertical gap between the pyrrolic N and β-C atoms, respectively. **Figure S17** serves as an example of the optimized configuration.

First of all, it must be noted that the *L*(Co) value is independent of the initial conditions. Therefore, all configurations may be compared directly.

For all aggregates constructed from the C_{4h} isomer, the optimized φ value is equal to the preset one. The fully staggered C_{4h}–C_{4h} (right–left) configuration with E = -844 kJ/mol is energetically favorable, while a barrier between it and the fully eclipsed one is very low (as E = -797 kJ/mol for the intermediate case with φ of

15 ° indicates). The *L*(Pc) distances are large for both fully staggered C_{4h}–C_{4h} configurations, indicating that the sterical repulsion rather than the π–π-attraction controls the aggregate structure.

Table. Calculated characteristics of the bimolecular aggregates of CoPc[#].

Molecular Set C_{4h}–C_{4h} (right–left)					
φ	*L*(Co)	*L*(Pc)			-*E*
		Max	Min	Av	
0	2.55	3.69	3.11	3.41	828
15	2.55	3.81	3.11	3.53	797
45	2.54	4.01	3.31	3.55	844
Molecular Set C_{4h}–C_{4h} (right–right)					
φ	*L*(Co)	*L*(Pc)			-*E*
		Max	Min	Av	
0	2.54	3.81	3.10	3.42	724
45	2.54	3.84	3.36	3.52	724
Molecular Set D_{2h}–D_{2h}					
φ	*L*(Co)	*L*(Pc)			-*E*
		Max	Min	Av	
2.5	2.53	3.77	3.06	3.48	687
38.0	2.55	3.62	3.22	3.33	1126

Abbreviations: φ, the rotation angle, deg; *L*(Co), the Co–Co distance, Å; *L*(Pc), the Pc–Pc distance, Å; *E*, the binding energy, kJ/mol.

A key result was obtained for the D_{2h}–D_{2h} molecular set (**Table**, bottom). In both configurations, the preset and optimized φ values are not equal and the primary amine groups of the bound molecules are finely fitted to one another (**Figure S18**).

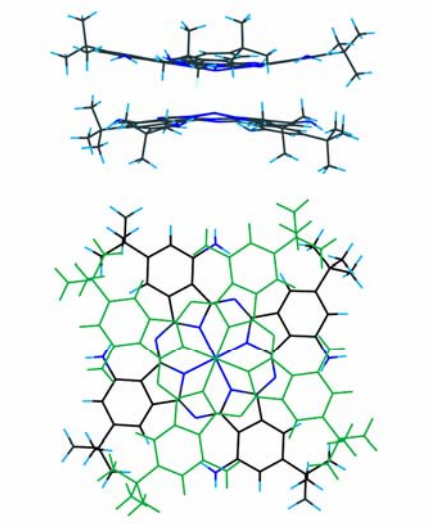

Figure S17. Optimized configuration of the CoPc[#] aggregate constructed from two C_{4h} isomer molecules with the primary amine groups facing to left (black) and right (green).

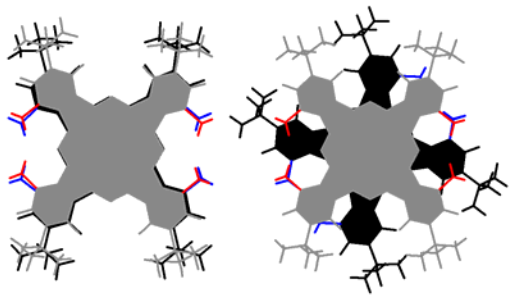

Figure S18. Optimized staggered configurations of the bimolecular aggregate constructed from the D_{2h} isomer of CoPc[#]. The primary amine groups are drawn with blue and red for the top and bottom molecules, respectively.

The staggered D_{2h}–D_{2h} configuration with φ of 38 ° and two mutually fitted amine groups is very stable (as *E* = -1126

kJ/mol indicates). Besides, the smallest difference between the maximal and minimal *L*(Pc) values (3.62 Å and 3.22 Å, respectively) indicates that the macrocycle is distorted to a lesser degree than in all other cases.

Part IV. Morphology vs. C_{60} Content

Three LS films were prepared in this work: the pristine dye film and two composite ones with the Pc/C_{60} ratio of ca. 1:2 and ca. 1:6.

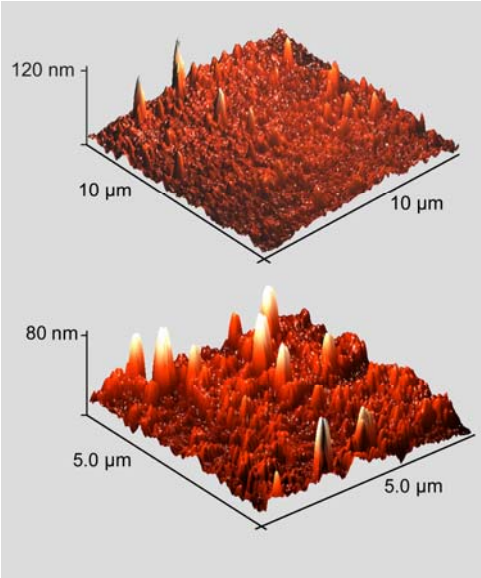

Figure S19. Perspective AFM images of the pristine dye film. The top image presents a general view; the bottom image allows observing the lateral fusion of small cone-shaped protrusions.

Figure S19 shows two typical locations in the pristine dye film. A key morphological feature is a giant (80–120 nm in height) 3D protrusion. Firstly this kind of a nanostructure was observed in LB films of an amphiphilic organic dye. [S10]

The top image shows a location without visible marks of the shear stress, thus indicating that the giant protrusions were developing spontaneously. A close inspection of the bottom image allows one to observe an earlier stage of the protrusion formation, namely, the lateral fusion of minor (20–30 nm in height) cone-shaped ones.

When moderate quantities of fullerene C_{60} are added to the system, the film acquires new features. **Figure S20** demonstrates all kinds of C_{60}-bond defects visually detectable in the key composite film.

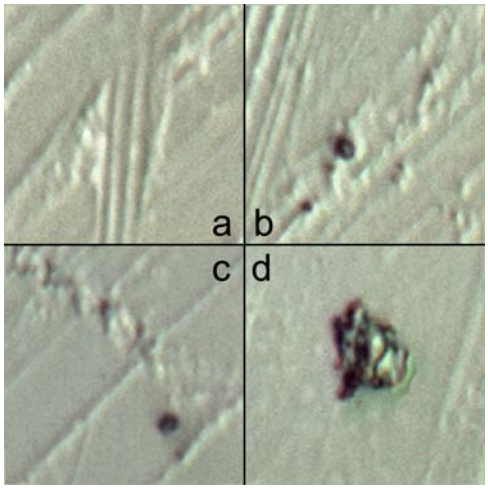

Figure S20. Zoom-in optical images (20×20 μm) of the key composite films (CoPc$^{\#}$/C_{60} ca. 1:2, mol; 30 layers). See the text for explanation.

Figure S20a shows a location, which was severely bitten by the gas flow but sustained the phase separation. Such locations occupy nearly the whole film surface

(ca. 99%). **Figure S20b** shows the most typical defect, an isolated C_{60}-rich pool of ca. 3 μm in diameter. Besides, several weakly pronounced pools are discernible around. All pools are located within the grooves. The same feature was observed in our work [S4], where the composite β-benzyl-naphthalene–C_{60} (1:1, mol) was prepared and analyzed. To be more specific, the copious homomolecular C_{60} aggregates were registered within the grooves by both optical microscopy and SAXS techniques. **Figure S20c** presents a location, where a pool rests over the film surface rather than within a groove. **Figure S20d** shows a huge pool with the visually observable interior. One may observe creases, which are lighter than the film surface due to the relatively weak light absorbance.

A scrupulous study of the key composite by AFM has allowed us to find out morphological patterns, which can be correlated with the said microdefects. The top image in **Figure S21** corresponds to **Figure S20a**: the film was dissected down to the glass surface but the phase separation did not occur. The bottom image presents a typical C_{60}-rich pool with two specific features of its interior. First, the film is 5–10 nm thick, i.e., by a factor of ca. 3 thinner than its intact portions. Second, the creases are constructed from cone-shaped protrusions (50–80 nm in height), which are not susceptible to the lateral fusion. Note: both features are lacking in the top image.

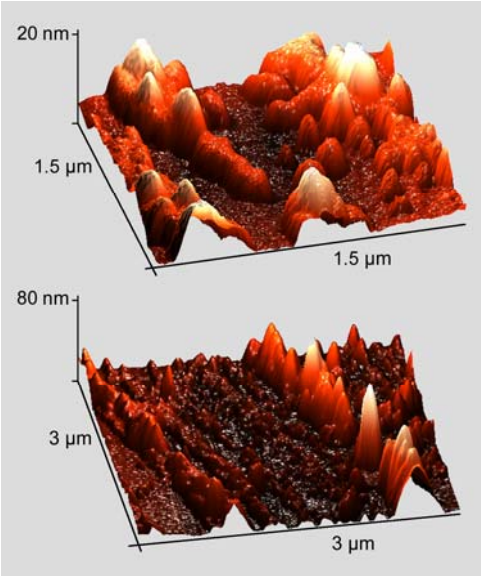

Figure S21. Perspective AFM images of the film shown in **Figure S20**. The top image shows a location, where two grooves are crossed at a sharp angle; the bottom image allows observing the interior of a C_{60}-rich pool.

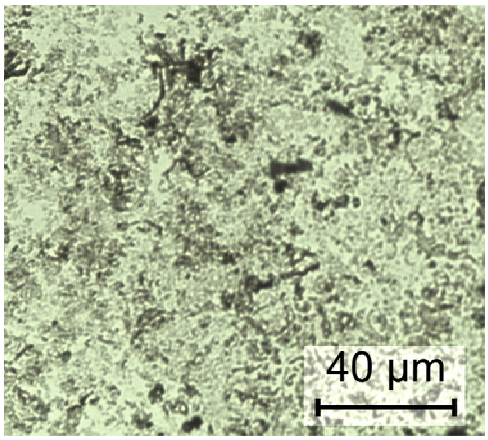

Figure S22. Optical microscopy image of the composite film ($CoPc^{\#}/C_{60}$ ca. 1:6, mol; 30 layers).

Frustratingly the composite film with the highest C_{60} content (Pc/C_{60} ~ 1:6) was

found to be rather featureless: only shapeless agglomerates are discernable in **Figures S22** and **S23**. Such a primitivism is obviously connected with the mainly mineral nature of the composite and, hence, low plasticity at all stages of the film formation. In contrast with the key composite film, the C_{60}-rich composite tends to flake off due to the poor adhesion to the hydrophilic glass surface.

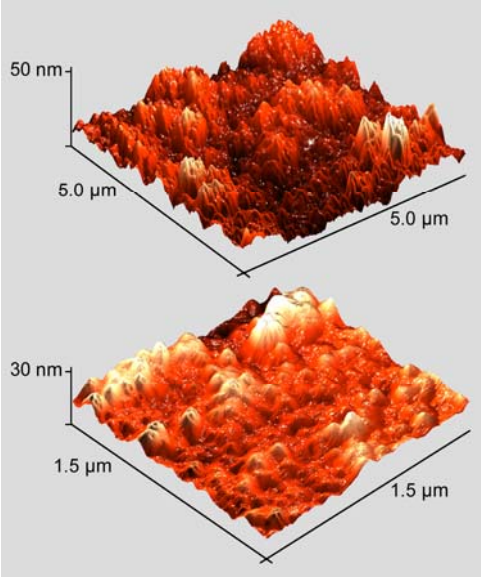

Figure S23. Perspective AFM images of the film shown in **Figure S22**.

In conclusion, the phase separation in the binary $CoPc^{\#}$–C_{60} (1:2, mol) composite film has been studied in detail by a combination of visible microscopy and AFM. Though strongly triggered by the shear stress, it originates principally from the irregular distribution of fullerene C_{60} rather than thermodynamic instability of the solid $CoPc^{\#}$–C_{60} system. Resistance of the composite $CoPc^{\#}$–C_{60} (1:2, mol) to the shear stress is by far higher than that of the composite β-benzyl-naphthalene–C_{60} (1:1, mol) [S4], indicating a crucial role of supramolecular H bonding as a structure forming interaction.

References

(S1) Web site of the A. V. Shubnikov Institute of Crystallography of the Russian Academy of Sciences: http://www.crys.ras.ru/~saxlab/experiments.html; accessed on 11/02/2013.

(S2) Kimura, M.; Kuroda, T.; Ohta, K.; Hanabusa, K.; Shirai, H.; Kobayashi, N. Self-organization of Hydrogen-bonded Optically Active Phthalocyanine Dimers. *Langmuir* **2003**, *19*, 4825–4830.

(S3) Valkova, L.; Borovkov, N.; Pisani, M.; Rustichelli, F. Structure of Monolayers of Copper Tetra-(3-Nitro-5-*tert*-butyl)-phthalocyanine at the Air–Water Interface. *Langmuir* **2001**, *17*, 3639–3642.

(S4) Borovkov, N.; Valkova, L.; Ol'khovich, M.; Glibin, A.; Koifman, O.; Zakharov, A. Fullerene–Naphthalene Interaction on the Water Surface and in the Binary Film. Fullerenes Nanotubes Carbon Nanostructures **2007**, *15*, 467–484.

(S5) Hato, M. Attractive Forces between Surfaces of Controlled “Hydrophobicity” across Water: A Possible Range of “Hydrophobic Interactions” between Macroscopic Hydrophobic Surfaces across Water. *J. Phys. Chem.* **1996**, *100,* 18530–18538.

(S6) Eriksson, J. Ch.; Henriksson, U. Bridging-cluster Model for Hydrophobic Attraction. *Langmuir* **2007**, *23,* 10026–10033.

(S7) Kolker, A. M.; Borovkov, N. Yu. Three-dimensional Aggregation of Fullerene C_{60} at the Air–Water Interface. *Colloids Surf. A* **2012**, *414*, 433–439.

(S8) Holzwarth, A. R.; Schaffner, K. On the Structure of Bacteriochlorophyll Molecular Aggregates Chlorosomes of Green Bacteria. A Molecular Modeling Study. *Photosynth. Res.* **1994**, *41*, 225–233.

(S9) Coleman, W. F.; Arumainayagam, Ch. R. HyperChem 5. *J. Chem. Educ*. **1998**, *75*, 416.

(S10) Tachibana, H.; Yamanaka, Ya.; Matsumoto, M. Temperature effect on photochromic reaction in Langmuir–Blodgett films of amphiphilic spiropyran and their morphological changes. *J. Phys. Chem. B* **2001**, *105*, 10282–10286.